PCCP

Accepted Manuscript

ROYAL SOCIETY OF CHEMISTRY

www.rsc.org/pccp

Physical Chemistry Chemical Physics
CREATED USING THE RSC LaTeX PCCP ARTICLE TEMPLATE – SEE www.rsc.org/electronicfiles FOR DETAILS
ARTICLE TYPE www. rsc.org/xxxxxx | XXXXXXXX

The photocycle and ultrafast vibrational dynamics of bacteriorhodopsin in lipid nanodiscs

Philip J. M. Johnson,[a] Alexei Halpin,[a] Takefumi Morizumi,[b] Leonid S. Brown,[c] Valentyn I. Prokhorenko,[d] Oliver P. Ernst,[b,e] and R. J. Dwayne Miller*[a,d]

Received Xth XXXXXXXXXX 20XX, Accepted Xth XXXXXXXXX 20XX
First published on the web Xth XXXXXXXXXX 20XX
DOI: 10.1039/b000000x

The photocycle and vibrational dynamics of bacteriorhodopsin in a lipid nanodisc microenvironment have been studied by steady-state and time-resolved spectroscopies. Linear absorption and circular dichroism indicate that the nanodiscs do not perturb the structure of the retinal binding pocket, while transient absorption and flash photolysis measurements show that the photocycle which underlies proton pumping is unchanged from that in the native purple membranes. Vibrational dynamics during the initial photointermediate formation are subsequently studied by ultrafast degenerate transient absorption spectroscopy, where the low scattering afforded by the lipid nanodisc microenvironment allows for unambiguous assignment of ground and excited state nuclear dynamics through Fourier filtering of frequency regions of interest and subsequent time domain analysis of the retrieved vibrational dynamics. Canonical ground state oscillations corresponding to high frequency ethylenic and C-C stretches, methyl rocks, and hydrogen out-of-plane wags are retrieved, while large amplitude, short dephasing time vibrations are recovered predominantly in the frequency region associated with out-of-plane dynamics and low frequency torsional modes implicated in isomerization.

1 Introduction

The light-driven proton pump bacteriorhodopsin (bR) consists of an opsin apoprotein and a covalently bound retinal chromophore, which in the light-adapted state adopts an all-*trans* configuration[1]. Following absorption of a photon, the chromophore isomerizes to a 13-*cis* configuration, and a photocycle ensues resulting in the translocation of a proton across the purple membrane. This initial isomerization reaction has attracted continuous attention since the discovery of the subpicosecond kinetics of the isomerization event[2,3]. The vibrational dynamics relevant to the isomerization process involve ethylenic and single bond stretches, methyl rocking, hydrogen out of plane (HOOP) modes, and low frequency torsions. The decoherence of these modes is sufficiently long relative to the timescale of the photoisomerization process that they can still play a role in coherently driving the reaction. Recent weak field coherent control experiments[4,5] use such a framework to explain the enhancement or suppression of the quantum yield of isomerization through coupling of the excitation field to excited state vibrational modes involved in isomerization.

However, the very assignment of excited state vibrational modes remains controversial. Early experiments interpreted the coherent vibrational dynamics observed in ultrafast transient absorption measurements of bR as a primarily ground state effect[6,7], attributed to coherent wavepacket motion generated through a resonant impulsive Raman process, and as such are unrelated to the reactive dynamics. Subsequently, similar measurements with sub-5 fs pump and probe pulses[8] were analyzed under the exact opposite basis, that all the observed vibrational dynamics originate from the excited state, owing to the extremely short temporal profile of the excitation pulse[9]. In part because of the incompatibility of these two viewpoints, additional transient absorption[10,11], infrared emission[12], femtosecond stimulated Raman[13–15], and degenerate four wave mixing (DFWM)[16] measurements have been performed, each reaching somewhat different conclusions as to the specific nature of vibrational dynamics following ultrafast excitation.

To clarify the assignment of vibrational modes, we have employed lipid nanodiscs as the microenvironment in which to embed bR. Lipid nanodiscs[17] are a relatively new molecular platform for membrane-bound proteins (previously applied to both monomeric and trimeric bR[18], rhodopsin[19,20], and light-harvesting proteins[21], among others[22–24]), consisting of

[a] *Institute for Optical Sciences & Departments of Chemistry & Physics, University of Toronto, 80 St. George Street, Toronto, Ontario M5S 3H6, Canada.*
[b] *Department of Biochemistry, University of Toronto, 1 King's College Circle, Toronto, Ontario M5S 1A8, Canada.*
[c] *Department of Physics and Biophysics Interdepartmental Group, University of Guelph, 50 Stone Road East, Guelph, Ontario N1G 2W1, Canada.*
[d] *Max Planck Institute for the Structure and Dynamics of Matter, Atomically Resolved Dynamics Division, Building 99 (CFEL), Luruper Chaussee 149, 22761 Hamburg, Germany.*
[e] *Department of Molecular Genetics, University of Toronto, 1 King's College Circle, Toronto, Ontario M5S 1A8, Canada.*

nanoscale patches of lipid bilayer surrounded by membrane scaffold protein "belts", ensuring a monodisperse size distribution on the order of 10 nm (see Fig. 1). This is in marked contrast with the native purple membrane environment of bR, where the membranes have a characteristic length scale on the order of the wavelength of light used for the study of bR photochemistry, the result of which is parasitic optical scattering which limits the signal to noise ratio of spectral measurements. The nanoscale dimensions of the lipid nanodiscs dramatically reduce the optical scattering at visible wavelengths, allowing for clearer spectral signatures of vibrational dynamics.

Despite the obvious advantage of embedding a membrane-bound protein in a more native-like environment while maintaining the small monodisperse particle size to minimize scattering, only recently have the spectroscopic properties of photoactive proteins in nanodiscs been explored[21,23]. Other microenvironments have been applied to the study of bR in the past[25–27], where departures from native behaviour have been observed both in the kinetics of the photocycle and in the light adaptation process. For the more native-like lipid vesicles, variability in vesicle diameter has been observed between 80–1000 nm, and the optical scattering has shown similarly significant variation between preparations[25,26]. The monodisperse nature of the nanodiscs solve this problem with the membrane scaffold proteins specifying the size of the nanodiscs, but it is still important to fully characterize the effect of the nanodisc environment on the bR response to enable comparison to fully native conditions. Here, we use steady-state spectroscopy to characterize the light adaptation process and time-resolved spectroscopies to probe the subsequent photocycle dynamics, finding that while there are deviations in the kinetics of the millisecond photocycle intermediates, light adaptation and the primary photointermediate formation on a subpicosecond timescale are identical to those in the purple membranes. We then employ ultrafast degenerate transient absorption spectroscopy to study the vibrational dynamics of retinal following photoexcitation. Applying Fourier filters to isolate oscillatory frequencies of interest, direct analysis of the resultant oscillatory transients in the time domain allows for a more complete recovery and assignment of both ground and excited state vibrational dynamics.

2 Materials and methods

2.1 Sample preparation

MSP1D1E3 expression and purification was carried out as described previously[28]. Bacteriorhodopsin was initially solubilized with 4% w/v Triton X-100 from washed purple membrane isolated from *H. salinarum* cultures. For incorporation of bR in nanodiscs, the solubilized bR and MSP1D1E3 were mixed with 1-palmitoyl-2-oleoyl-*sn*-glycero-3-phosphocholine (POPC) lipids (Avanti Polar Lipids, Inc.) solubilized in 100 mM cholate to a final molar ratio of bR/MSP1D1E3/lipid of 3:2:100. The buffer for the nanodisc self-assembly and the following size exclusion chromatography consisted of 10 mM Tris/HCl, 0.1 M NaCl, pH 7.4 at 20°C. The mixture was incubated for 30 min. Subsequently, detergent was removed by treatment for 3 h at room temperature with 500 mg wet Biobeads SM-2 (Bio-Rad) per ml of solution, with gentle agitation to keep the beads suspended. Beads were removed by centrifugal filtration. Self-assembled nanodiscs were concentrated, filtered through 0.22 μm filters and injected onto a Superdex 200 10/300 GL column (GE Healthcare) run at 0.5 ml/min at room temperature with collection of 2 min fractions. Peak elution was monitored at 280 and 565 nm. The final sample was resuspended in 100 mM MES, 500 mM NaCl, pH 6.0, and was kept at room temperature for all subsequent measurements. Linear absorption and circular dichroism spectra (see Fig. 2) were used to confirm the trimeric nature of bacteriorhodopsin in lipid nanodiscs. The linear absorption maximum is consistent with native purple membrane bR (shown as the dashed line), with a significantly lower baseline due to a lack of scattering, while the circular dichroism spectrum shows a biphasic character about the linear absorption maximum, as expected for bR trimers and in contrast with the monophasic signal exhibited by bR monomers[18].

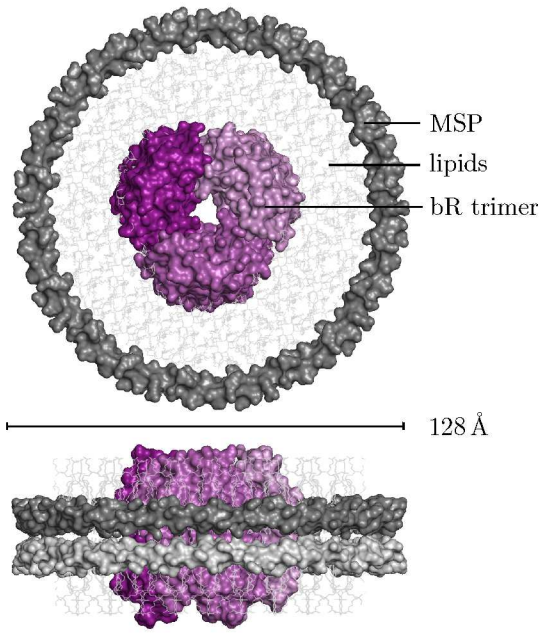

Fig. 1 Lipid nanodiscs with embedded trimeric bR. The nanodiscs consist of a small patch of lipid bilayer surrounded by membrane scaffold protein (MSP). The diameter of the trimeric bR nanodisc is 128 Å.

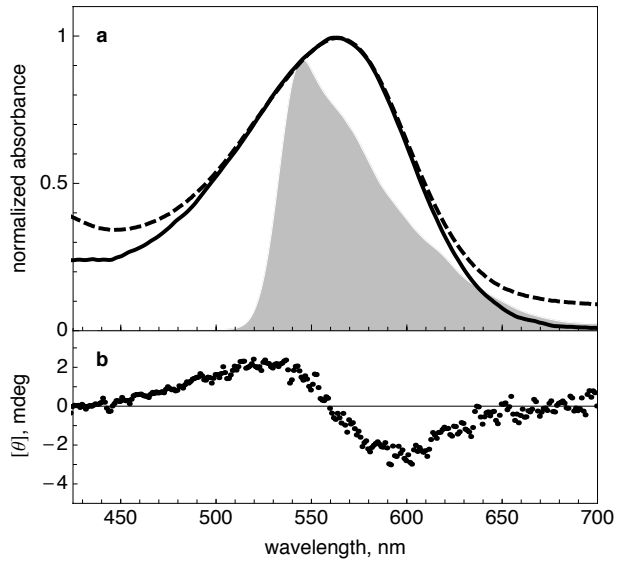

Fig. 2 Steady state spectroscopy of trimeric bR in lipid nanodiscs. a) The linear absorbance of nanodisc bR (solid line) is compared to purple membrane bR (dashed line), and displays the characteristic absorption maximum for light-adapted (all–*trans*) bR, while showing an extremely low scattering baseline compared to the purple membrane sample. The laser spectrum used for degenerate transient absorption experiments to measure the ultrafast vibrational dynamics of retinal during isomerization is shown filled in grey. b) The circular dichroism spectrum of trimeric bR in lipid nanodiscs features the characteristic biphasic response observed in the purple membranes.

2.2 Time resolved spectroscopy

2.2.1 Decay-associated spectra. Ultrafast spectrally-resolved transient absorption experiments to measure the population dynamics of bR were performed as described previously[29]. Briefly, ultrashort pulses used to excite the sample were generated by a noncollinear optical parametric amplifier (NOPA) at a central wavelength of 565 nm with 50 nm full width at half maximum (FWHM) bandwidth, and were subsequently compressed to a transform-limited 20 fs by a Dazzler (Fastlite) and folded SF11 prism pair compressor. A supercontinuum probe beam was generated in a 2 mm sapphire plate and compressed via multiple reflections on broadband chirped mirrors (Layertec). The pump and probe beams, having a polarization difference at the magic angle, were focused by an off-axis parabolic mirror into the sample, contained in a 400 μm pathlength rotation cell, where the sample OD was 0.25 at the absorption maximum of bR. Pump pulse energy at the sample position was 20 nJ, and the instrument response function (IRF) was 40 fs, determined by spectral integration of the nonlinear optical Kerr effect in a blank buffer cell. Transient absorption spectra were collected over the range [-0.5, 10] ps, with 20 fs time steps and an average of 128 differential measurements for each probe delay. Global analysis[30] of the transient absorption data was performed as described in Appendix A of Ref. 4. Experiments were performed at room temperature, with a halogen lamp continuously illuminating the sample to maintain the light-adapted state.

2.2.2 Flash photolysis. Long timescale intermediates of the bR photocycle were measured by time-resolved laser difference spectroscopy in the microsecond to second range, using a custom-built flash photolysis apparatus at room temperature[31]. The photocycle was initiated by flashes of the 532 nm second harmonic of a Nd:YAG Minilite II laser (Continuum), with a pulse duration of 7 ns. The probe beam was generated by an Oriel QTH source with a monochromator. The resulting absorbance changes at selected wavelengths were recorded using an Oriel photomultiplier, amplifier with a 350 MHz bandwidth, and a Gage AD converter (CompuScope 12100-64M). Several hundred traces were averaged and converted into a quasi-logarithmic timescale using in-house software. Global multi-exponential fitting was performed using FITEXP[32].

2.2.3 Ultrafast vibrational dynamics. To measure the coherent vibrational dynamics during isomerization, the pump and probe beams of the ultrafast transient absorption instrument described above were replaced with a broadband pulse (spectrum shown in Fig. 2a), compressed to ∼8 fs by a deformable mirror and prism compressor pair, as described previously[33]. The probe beam was generated via Fresnel reflection of the pump from a fused silica window (of similar intensity to the supercontinuum probe used previously), and both pump and probe beams were *p*-polarised. The IRF was determined, as above, to be 15 fs. Sample parameters were unchanged, while the excitation energy was decreased to 6 nJ. Transient signals were collected, as above, over the range [-0.5, 2] ps in 2.5 fs steps.

3 Photocycle in lipid nanodiscs

Absorption of a photon by the retinal chromophore in bR initiates a photocycle whereby the chromophore, initially in the all–*trans* configuration, isomerizes about the C_{13}=C_{14} bond to the 13–*cis* configuration on an ultrafast timescale producing the primary J and K intermediates. The remainder of the photocycle occurs on a much longer timescale (microseconds to seconds), where the energy stored in the 13-*cis* retinal is transferred to the protein (resulting in the L intermediate), inducing the Schiff base linkage between the retinal chromophore and the amino acid Lys216 to become deprotonated (formation of the M intermediate), thus allowing a proton to migrate across the purple membrane. The Schiff base is subsequently reprotonated (decay of the M and growth of the N intermediates), followed by thermal isomerization (via the O intermedi-

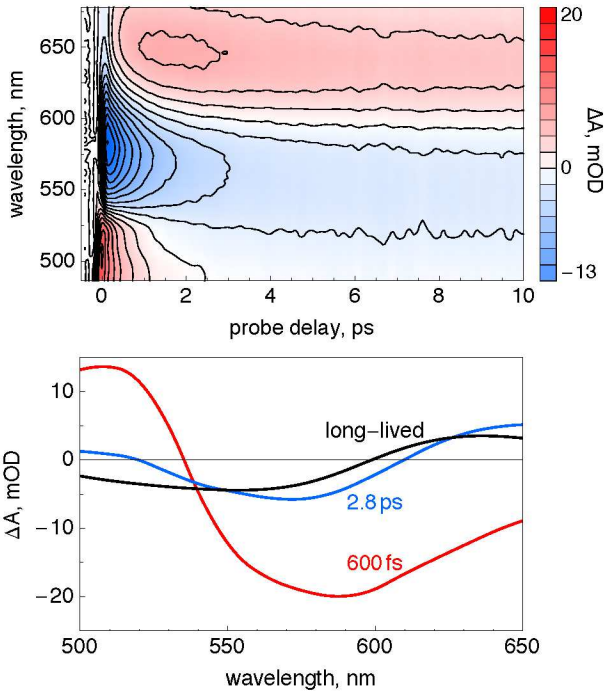

Fig. 3 Top: Spectrally resolved transient absorption measurements of the first 10 picoseconds of the nanodisc bR photocycle. Induced differential absorption corresponding to the primary bR photoproduct is observed at $\lambda \approx 630$ nm consistent with the response of purple membrane bR, concurrent with a negative bleach signal at the absorption maximum of bR. Excited state absorption to higher-lying energy surfaces is observed on the blue edge of our spectral window and decays within ~2 ps. Bottom: decay-associated spectral analysis of the time-resolved transient absorption data result in two dominant kinetic parameters with time constants of 0.6 and 2.8 ps, consistent with J and K photointermediate formation from purple membrane bR.

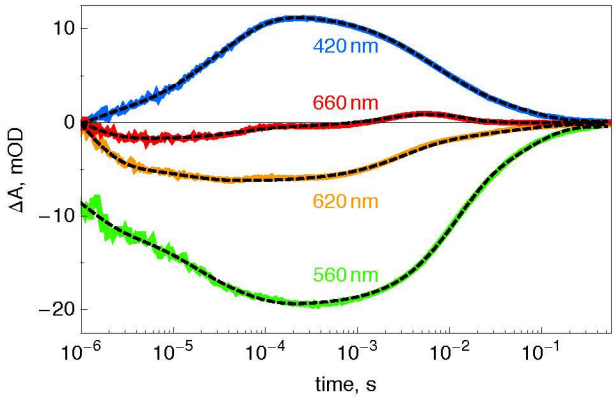

Fig. 4 Kinetics of the late photocycle intermediates of nanodisc bR from the absorption changes after laser flash excitation. The photocycle intermediates were followed at their characteristic wavelengths: M at 420 nm, O at 660 nm, and N and the ground state bleach signal at 560 nm. Additionally, the absence of the intermediates from a 13–*cis* bR cycle was verified at 620 nm. Dashed lines are the result of a six exponential global fit.

ate) of retinal back to the all–*trans* configuration, upon which the photocycle may begin anew.

To determine the influence of the lipid nanodisc microenvironment on the photocycle, we have probed the photocycle over more than ten orders of magnitude in time: on the ultrafast timescale by spectrally-resolved transient absorption to monitor the J and K intermediate formation, and on the microsecond to second timescale by laser flash photolysis to monitor the formation of the M, N, and O intermediates, allowing for a complete characterization of the photocycle of bR in lipid nanodiscs.

The result of the ultrafast spectrally-resolved transient absorption experiment is shown in Fig. 3. Immediately following excitation we observe a strong ground state bleach (GSB) signal at the light-adapted bR absorption maximum, along with the characteristic excited state absorption (ESA) at shorter wavelengths, attributed to the transition of population from the S_1 to S_4 potential energy surfaces[34]. At longer wavelengths, we observe photoproduct formation at $\lambda \approx 630$ nm, consistent with the native photocycle of purple membrane bR.

A comparison to the kinetics of purple membrane bR can be performed more quantitatively with a global analysis of the spectrally-resolved transient absorption data. The retrieved decay-associated spectra (DAS) show two main kinetic components: 0.6 ps and 2.8 ps, which can be attributed to the J and K intermediates, respectively. A long-lived background is present due to the finite temporal window over which we measure the transient signal. The DAS are fully consistent with previous measurements of the early bR photocycle[5,29] over a similar temporal window, indicating that the nanodisc microenvironment has no significant effect on the isomerization of retinal on the ultrafast timescale.

To further verify the native-like properties of bR trimers in lipid nanodiscs, we measured kinetics of the late photocycle intermediates in the microsecond to second time range at their characteristic wavelengths (see Fig. 4). The rise and decay of the M intermediate (corresponding to the deprotonation and reprotonation of the retinal Schiff base) was measured at 420 nm, the O intermediate (reflecting thermal isomerization of retinal back to the all–*trans* configuration) was detected at 660 nm, and the bleaching of the ground state (with added contribution from the N intermediate) was measured at 560 nm. Overall, the photocycle kinetics are very similar to those known for bR in the purple membrane. However, the reprotonation of the Schiff base (decay of the M intermediate) and the photocycle turnover occur somewhat slower than in the native bR, and the accumulation of the O intermediate is low for the

mildly acidic conditions of the nanodisc suspension[35,36].

The multi-exponential global fitting of the kinetics confirms the native-like character of the Schiff base deprotonation (formation of the M intermediate) on the microsecond timescale. The obtained time constants (1, 12, and 47 μs in a six exponential approximation) are close to those known for the purple membranes under similar conditions and signify normal transfer of proton from the Schiff base to its primary acceptor in the L→M reaction. However, all the processes related to the reprotonation of the Schiff base and resetting of the photocycle (M→N→O→bR) in the millisecond time domain (with the characteristic time constants of 3, 10, and 65 ms in the six exponential approximation) are several fold slower than the corresponding processes in the native bR[37,38]. This is not uncommon for monomeric bR in detergents or upon reconstitution into non-native lipids and does not imply any serious abnormalities in the photocycle[39,40].

We also confirmed that the nanodisc bR light adapts normally and does not produce intermediates from a 13–*cis* photocycle. First, the light adaptation was verified by the ∼10 nm redshift of the static absorption spectrum upon illumination with white light (recall Fig. 2a), reflecting production of a light-adapted all–*trans* bR. Second, the photocycle kinetics were monitored at 620 nm (Fig. 4) to verify the absence of the so-called C intermediate, a product of 13–*cis* bR[41,42], and no positive absorption changes were observed at this wavelength, confirming the complete light adaptation. Thus, the retrieved kinetics of the late photocycle intermediates combined with the normal light adaptation attest to the native behaviour of bR in the lipid nanodisc microenvironment.

The observation of slower late photocycle kinetics for nanodisc bR trimers is somewhat puzzling given that the similar effect in monomeric bR is attributed to the loss of protein-protein interactions afforded by the wild type aggregations. However, monomeric bR also exhibits spectral shifts in the absorption maximum of the ground state, indicative of structural differences in the retinal binding pocket, and possibly in the global folded structure as well. We observe no spectral shifts in the nanodisc bR assemblies, but the slower kinetics of the late photocycle may implicate structural difference in the protein which do not affect the binding pocket, and, thus, the ultrafast photochemistry. This interpretation is corroborated by recent structural solution NMR studies of bR in nanodiscs[43], which show that while the retinal binding pocket is effectively unchanged from the native structure in the purple membranes when reconstituted in lipid nanodiscs, deviations from the native fold in the EF loop region are observed. It is this region which has been previously implicated as the location of large conformational changes in the late photocycle intermediates[44,45], which may explain the deviations we observe in kinetics for the reprotonation of the Schiff base and resetting of the photocycle on the millisecond timescale.

4 Vibrational dynamics

With confirmation that the ultrafast isomerization dynamics of bR trimers in lipid nanodiscs reflect native behaviour, we turn our attention to the assignment of excited and ground state vibrational dynamics via conventional ultrafast transient absorption measurements. Transient absorption spectra were collected in the degenerate configuration using an ∼8 fs pulse with the spectrum shown in Fig. 2a, having sufficient temporal resolution and spectral bandwidth to excite and detect all of the relevant high frequency vibrational modes associated with retinal isomerization, while simultaneously monitoring the ground state bleach, excited state absorption, and photoproduct formation dynamics in a single measurement. The result of this measurement is shown in Fig. 5 (top panel), where we highlight the first picosecond following photoexcitation. At this high temporal resolution, coherent oscillations reflecting vibrational dynamics of the retinal chromophore are clearly visible over the entire temporal and spectral window of the transient response.

Two spectral regions of interest are highlighted as single wavelength traces in Fig. 5 (bottom panel, taken at the dashed lines in the top panel) at 525 nm and 630 nm, reflecting the excited state absorption and photoproduct formation bands, respectively. At the photoproduct absorption wavelength (red trace), the ground state bleach signal gives way to the primary photointermediate absorption on a $\sim$ 200 fs timescale, and coherent oscillations modulate the transient spectral response at this wavelength over the entire first picosecond shown here. Dynamics at the wavelength associated with the excited state absorption (blue trace) display an effectively instantaneous absorptive feature which persists for $\sim$ 200 fs before giving way to the ground state bleach, with large amplitude oscillatory features modulating the transient response. At both probe wavelengths these features are observed to decay in amplitude as a function of the probe delay.

To assign the oscillatory dynamics to either ground or excited state vibrations it is necessary to determine both their frequencies and dephasing times. The most common method employed for this purpose has been a sliding window Fourier analysis of the time domain transients, where a short section of the time domain data is windowed with a suitable (e.g. Hanning[8,12], super-Gaussian[10,16], or Blackman[11]) filter, and subsequently Fourier transformed to reveal the frequencies of the windowed oscillatory data. This approach, however, has inherent limitations: obtaining the frequency resolution required to distinguish the many closely spaced vibrations of the retinal chromophore necessarily results in a poor temporal resolution. Conversely, maintaining a high temporal resolution to accurately gauge the vibrational dynamics during isomerization results in artifacts in the frequency domain[16]. It is also difficult to treat the very earliest transient response using this

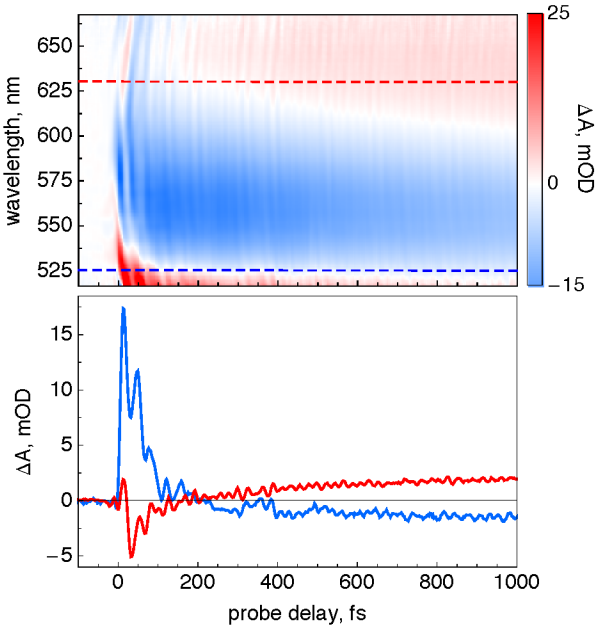

Fig. 5 Vibrational dynamics of the retinal chromophore in bR revealed by high temporal resolution transient absorption spectroscopy. Top: Spectrally-resolved transient absorption response with 8 fs pump and probe pulses showing coherent oscillatory dynamics over the entire spectral and temporal window afforded by the excitation and detection beams. Bottom: single wavelength traces at 525 nm (blue) and 630 nm (red), representing spectral response associated with excited state absorption and photoproduct formation, respectively.

approach, despite the vibrational modulations being maximal immediately following photoexcitation.

We overcome these limitations by performing all analyses of oscillatory transients in the time domain, taking advantage of the high temporal resolution of the measurement. Still, however, the large number of closely spaced vibrations precludes direct quantitative analysis of the single wavelength traces of the vibrational response. As determined by previous sliding window analysis, these vibrations are clustered in distinct frequency regions, such as ethylenic and other double bond stretches between 1500–1700 cm^{-1}, single bond stretches and associated rocking dynamics between 1100–1300 cm^{-1}, methyl rock and HOOP modes between 800–1000 cm^{-1}, and low frequency bends and torsions with frequencies below 500 cm^{-1}. To isolate these dynamics, Fourier filtering in the frequency domain is employed to isolate each of these regions of interest with a tapered cosine window (also called a Tukey window[46]) of the form

$$w(n) = \begin{cases} 1, & 0 \le |n| \le \alpha\frac{N}{2} \\ \frac{1}{2}\left(1+\cos\left[\frac{\pi(n-\alpha\frac{N}{2})}{(1-\alpha)\frac{N}{2}}\right]\right), & \alpha\frac{N}{2} \le |n| \le \frac{N}{2} \end{cases}$$

which, owing to the flat top, conserves the amplitudes of Fourier components of interest over a greater frequency range than a cosine or Gaussian window, while still limiting artifacts arising from a pure square bandpass filter. We use a tapered cosine window with $\alpha = 1/3$ and a FWHM in the Fourier domain of $\sim$350 cm^{-1} ($N \sim 62$ discrete frequency points, with a resolution of ~ 8.3 cm^{-1} following zero padding by a factor of two), parameters chosen to allow for filtering of the frequency ranges of interest described above without significant overlap between neighbouring filters.

The result of this process is shown in Fig. 6 for both single wavelength traces highlighted previously, where now the slow population dynamics have been subtracted leaving only the coherent vibrational dynamics of the retinal chromophore. To adequately reconstruct the data, five separate filters were applied at central frequencies of 1580, 1250, 910, 580, and 260 cm^{-1}, shown in the bottom panel of Fig. 6. The summation of all five of the filtered transients for each respective wavelength is shown superimposed as the black dashed line in the top panels, showing excellent agreement for both the 630 and 525 nm probe wavelength traces.

Some qualitative features of the filtered vibrational traces warrant immediate discussion. First, somewhat surprisingly, the inclusion of filtered oscillatory transients at a central frequency of ~ 580 cm^{-1} was required to realize good agreement with the raw data, a frequency range little discussed in terms of retinal isomerization, at least with respect to ground state modes[47,48]. Second, a spectral dependence of the amplitudes of the oscillatory transients was observed, where oscillations in the probe region associated with the excited state absorption at 525 nm were found to have significantly larger amplitudes, particularly so for oscillations with frequencies at and below those of the methyl rocking and HOOP modes. Third, in almost all cases a beat pattern is observed, indicating multiple closely spaced frequencies resulting in interference in the time domain. One distinct exception is the recovered oscillatory transient associated with highest frequency ethylenic stretching when probing at 630 nm. This oscillation shows a minimal beat pattern over the 1 ps window shown in Fig. 6, implicating a single dominant mode. It is this exact spectral region where distinctly ground state ethylenic stretches have been observed previously[49], and we find good qualitative agreement in the present data.

The fact that the other traces display markedly different dynamics requires a more complete and quantitative analysis. With the reduction in the number of oscillatory transients per filtered trace, nonlinear fitting of the time domain data becomes possible. For all ten filtered oscillations shown in Fig. 6, we fit a sum of damped sinusoids of the form $\sum_i A_i e^{-t/\tau_i} \sin(2\pi\nu_i t + \phi_i)$, where all amplitudes, dephasing times, frequencies, and phases remain free parameters, and the number of components is increased until the standard devia-

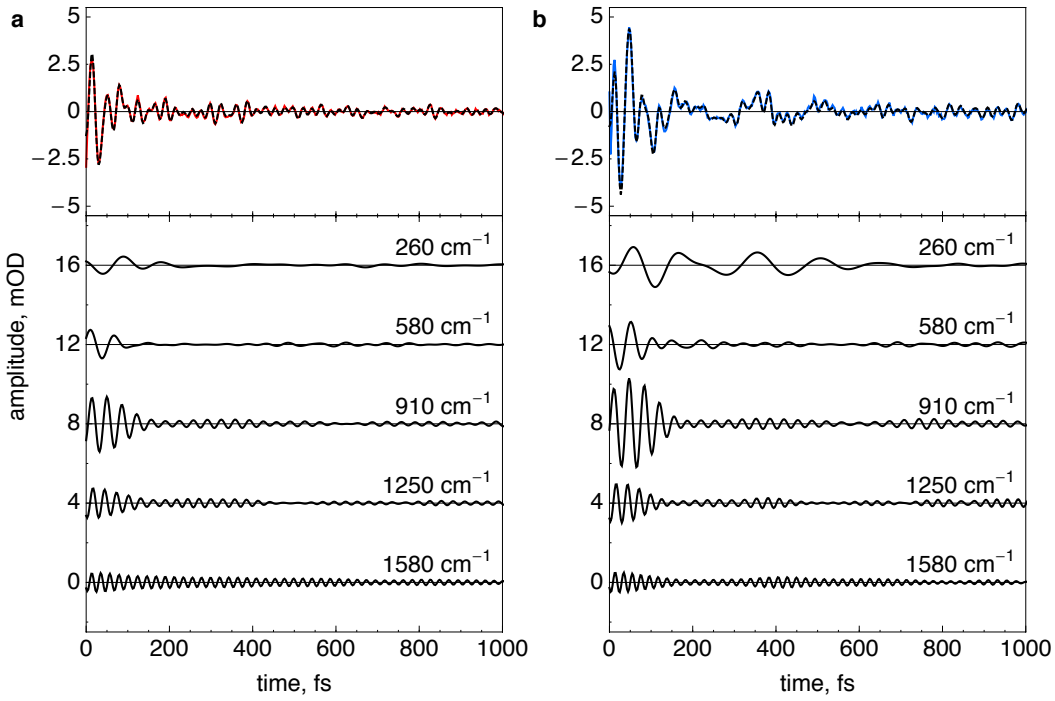

Fig. 6 Retrieved time-domain vibrational transients from Fourier filtering of single wavelength traces. The top panels show the background-subtracted data (solid coloured lines) for both the a) 630 nm and b) 525 nm single wavelength traces. The application of tapered cosine windowing at various central frequencies in the Fourier domain is shown in the bottom panels, with the sum of all five filtered transients shown in the top panel (as the superimposed dashed lines), highlighting the excellent agreement between the summation of filtered transients and the raw data. Significantly higher amplitude vibrational transients are observed at the excited state absorption band at 525 nm, and in almost all cases a beat pattern is observed, indicating multiple closely spaced frequencies underlying each trace. A notable exception is the highest frequency oscillations at the 630 nm probe wavelength.

tion of the residuals of the fit are $\leq 3\%$ of the signal maximum. One example of this procedure is shown in Fig. 7, where the oscillatory transients retrieved following the application of a tapered cosine window at 1580 cm^{-1} for $\lambda = 630$ nm (top panel, solid red line) are fit to a sum of nine damped sinusoids (superimposed dashed black line), resulting in a std of residuals of 2.01%. The corresponding power spectra for both the filtered transients and the fit function are shown in the bottom panel of Fig. 7, showing that the goodness of fit in the time domain carries to the frequency domain, giving confidence in this procedure to extract the relevant frequencies, amplitudes, and dephasing times of the constituent vibrational modes.

The result of this analysis for all filtered vibrational modes at $\lambda = 630$ nm are listed in Table 1, while the retrieved oscillations at $\lambda = 525$ nm are listed in Table 2. While there are many weak but long-lived oscillations retrieved by the fit procedure (and are evident in the power spectra), we are most interested in those oscillations which dominate the vibrational response at early times, and thus only report modes with initial amplitudes $A_i \geq 0.1$ mOD, a value which corresponds to approximately twice the noise floor of the time domain measurement. The retrieved amplitudes and dephasing times show great variability between vibrations, and are the principle means we employ of classifying a mode as ground or excited state in origin. In the case of long dephasing time modes, concurrence with known ground state oscillations from resonance Raman scattering[47,48] are highlighted. The retrieved vibrations are outlined from high to low frequency.

4.1 High frequency stretches: 1400–1700 cm^{-1}

630 nm. The dominant high frequency mode retrieved from the oscillations at 630 nm (Fig. 7) is the canonical ground state ethylenic stretch vibration at 1522 cm^{-1} with a dephasing time of 459 fs, previously determined[48] to be the symmetric stretch of the doubled-bonded carbons along the retinal polyene chain.

525 nm. The symmetric ethylenic stretching mode with a dephasing time on the order of half a picosecond again figures prominently at the probe trace at 525 nm, identical within error of the retrieved fit parameters to the vibration recovered in the red. Unlike the response at 630 nm, however, additional

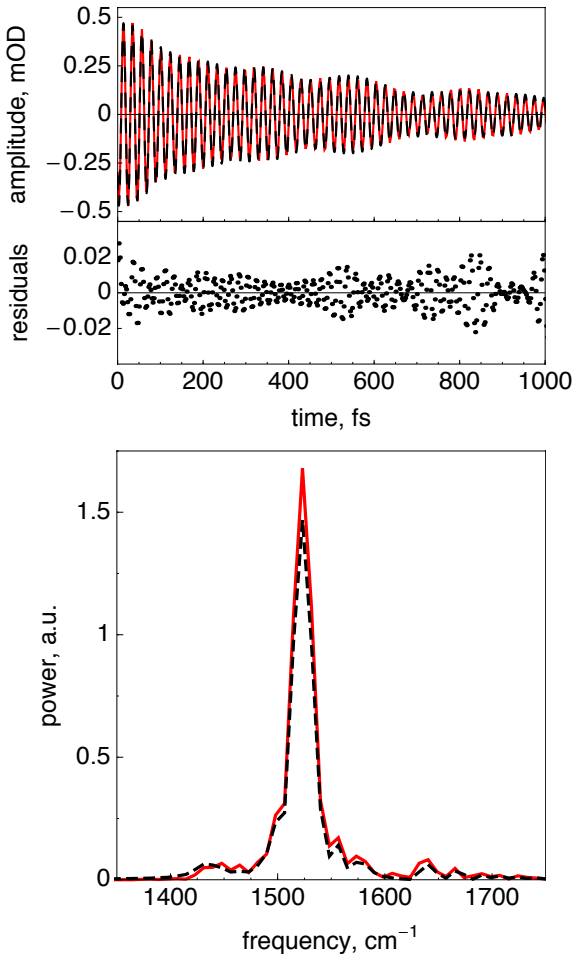

Fig. 7 Top: filtered data (red trace) and a nine component fit (dashed black line) to the highest frequency oscillatory transients at the 630 nm probe wavelength from Fig. 6, with residuals of the fit shown immediately below. Bottom: power spectra of both the filtered data (red line) and the fit function (dashed black line).

modes with significant initial amplitude are present. We observe a combination band[48] at 1544 cm^{-1} with a dephasing time of 482 fs, and a large amplitude mode at 1633 cm^{-1} with a short dephasing time of only 234 fs, a feature observed previously in transient IR spectroscopy of purple membrane bR[50] in the frequency region associated with the C=N bond of the Schiff base.

4.2 C-C stretches and associated rocks: 1050–1350 cm^{-1}

630 nm. Four modes are retrieved in the frequency range associated with single bond stretches and rocks. Two conventional ground state oscillations are found at 1265 and 1198 cm^{-1}, both with dephasing times on the order of 800 fs. From previous Raman measurements[48], the mode at 1265 cm^{-1} can

Table 1 Large amplitude vibrational modes recovered from time domain analysis of Fourier filtered transients at $\lambda = 630$ nm.

ν_i, cm^{-1}	A_i, mOD	τ_i, fs	ϕ_i, rad
1522 ± 2	0.51 ± 0.04	459 ± 84	4.1 ± 0.1
1265 ± 1	0.10 ± 0.01	711 ± 82	5.2 ± 0.1
1198 ± 1	0.11 ± 0.01	821 ± 81	4.8 ± 0.1
1171 ± 1	0.57 ± 0.02	277 ± 7	4.2 ± 0.1
1092 ± 5	0.75 ± 0.07	91 ± 7	3.8 ± 0.1
1008 ± 1	0.27 ± 0.01	604 ± 25	3.2 ± 0.1
854 ± 3	1.91 ± 0.07	65 ± 3	0.2 ± 0.1
606 ± 1	0.50 ± 0.04	146 ± 12	0.5 ± 0.1
554 ± 20	0.30 ± 0.16	455 ± 24	5.4 ± 0.5
419 ± 2	0.13 ± 0.01	345 ± 37	1.1 ± 0.1
313 ± 3	0.14 ± 0.09	664 ± 23	3.9 ± 0.6
297 ± 8	0.25 ± 0.07	373 ± 22	2.4 ± 0.3

been attributed to either a $C_{11}H$ rocking (observed at 1273 cm^{-1}) or a lysine rock (observed at 1255 cm^{-1}), while the vibration at 1198 cm^{-1} has been identified as single bond stretching of C_{14}-C_{15} and C_8-C_9 coupled with $C_{10}H$ and $C_{15}H$ rocking motion. Two short dephasing time modes are also observed at 1171 and 1092 cm^{-1}, with dephasing times of 277 and 91 fs, respectively. The mode at 1092 cm^{-1} has not previously been observed by Raman scattering, while the mode at 1171 cm^{-1} has previously been assigned to C_{10}-C_{11} and C_8-C_9 stretches coupled to rocking motion due to $C_{11}H$ and $C_{12}H$.

525 nm. Oscillatory transients at this frequency range appear quite distinctly as a number of short dephasing time excited state modes. These are observed at 1097 and 1220 cm^{-1} with dephasing times of 217 and 267 fs, respectively. As for the equivalent mode in the red, the retrieved vibration at 1097 cm^{-1} has previously not been observed, while the 1220 cm^{-1} mode is in the frequency region associated with C_8-C_9 stretching. Additional prominent modes having dephasing times between 500-800 fs are observed at 1281, 1165, and 1254 cm^{-1}, and can be assigned[48] to the well known ground state oscillations resulting from $C_{11}H$ and $C_{12}H$ dynamics, C_{10}-C_{11} stretches, and C_{12}-C_{13} stretches coupled to lysine rocking dynamics, respectively.

4.3 Methyl rocking and HOOP modes: 700–1050 cm^{-1}

630 nm. Vibrations in the frequency region associated with in- and out-of-plane methyl rocking and hydrogen wags are represented by two distinct modes: the ground state methyl rock at 1008 cm^{-1} with a dephasing time of 604 fs, and a short-lived mode ($\tau = 65$ fs) at 854 cm^{-1}, a mode which is not consistent with any known ground state mode of bR.

525 nm. In contrast with the response at 630 nm, many modes are retrieved at 525 nm. Of these, two modes are in

Table 2 Large amplitude vibrational modes recovered from time domain analysis of Fourier filtered transients at $\lambda = 525$ nm.

ν_i, cm^{-1}	A_i, mOD	τ_i, fs	ϕ_i, rad
1633 ± 1	0.24 ± 0.02	234 ± 14	3.8 ± 0.1
1544 ± 2	0.22 ± 0.03	482 ± 54	3.3 ± 0.3
1522 ± 1	0.22 ± 0.03	606 ± 61	5.4 ± 0.1
1281 ± 1	0.22 ± 0.01	593 ± 20	4.4 ± 0.1
1254 ± 1	0.16 ± 0.01	616 ± 31	3.8 ± 0.1
1220 ± 1	0.48 ± 0.02	267 ± 8	3.2 ± 0.1
1165 ± 1	0.18 ± 0.02	786 ± 59	0.1 ± 0.1
1097 ± 2	0.51 ± 0.03	217 ± 11	4.9 ± 0.1
1008 ± 1	0.26 ± 0.07	815 ± 15	5.0 ± 0.1
971 ± 1	1.62 ± 0.07	189 ± 4	5.1 ± 0.1
940 ± 1	0.61 ± 0.03	355 ± 10	3.4 ± 0.1
882 ± 1	0.10 ± 0.01	866 ± 39	3.6 ± 0.1
869 ± 2	2.62 ± 0.08	75 ± 2	0.7 ± 0.1
834 ± 12	0.17 ± 0.02	768 ± 62	5.5 ± 0.5
734 ± 2	0.13 ± 0.05	435 ± 78	6.1 ± 0.4
564 ± 16	1.39 ± 0.27	64 ± 15	2.6 ± 0.2
354 ± 2	0.17 ± 0.04	465 ± 62	4.4 ± 0.2
328 ± 2	0.32 ± 0.06	345 ± 37	4.2 ± 0.2
293 ± 1	0.16 ± 0.02	742 ± 61	5.3 ± 0.1
226 ± 2	1.17 ± 0.09	298 ± 21	5.0 ± 0.1
195 ± 1	1.10 ± 0.08	247 ± 11	1.9 ± 0.1

good concurrence with those above. The methyl rock at 1008 cm^{-1} is also present at this probe wavelength, with a similarly long dephasing time of 815 fs. We also retrieve a very short-lived mode ($\tau = 75$ fs) at 869 cm^{-1}, again consistent with the mode observed at 630 nm. An additional large amplitude, short-lived mode is observed at 971 cm^{-1} ($\tau = 189$ fs), which is not readily assignable to a ground state oscillation. Four longer dephasing modes are retrieved at 940, 882, 834, and 734 cm^{-1}, of which the first three are readily assigned to dynamics resulting from the NH wag coupled to the lysine residue, HOOP wags at C_{14}, C_{12}, and C_{11}, and HOOP activity at C_{11}, C_{12}, C_{15}, and the lysine and NH bond, respectively[48].

4.4 Low frequency vibrations: $\leq$700 cm^{-1}

630 nm. Below 700 cm^{-1}, five vibrations are retrieved with sufficient amplitude to affect the early transient vibrational dynamics. Two of these modes have dephasing times in excess of 450 fs, at 554 and 313 cm^{-1}, while the remaining three modes have dephasing times indicating, perhaps, excited state character. These are found at 606, 419, and 297 cm^{-1}, with dephasing times of 146, 345, and 373 fs, respectively. While we know of no specific source for the assignment of low frequency modes in bR, similar analysis of the low frequency vibrations in all-*trans* retinal[51] suggest that oscillations in this frequency range reflect delocalized chain bending and ring torsional dynamics.

525 nm. Six modes are found below 700 cm^{-1} at the probe wavelength associated with the excited state dynamics, and these oscillations represent some of the largest amplitude vibrations of the retinal chromophore. These are modes at 564, 226, and 195 cm^{-1}, all with short dephasing times indicative of excited state dynamics at 64, 298, and 247 fs, respectively. An additional lower amplitude and shorter dephasing time mode is observed at 328 cm^{-1} ($\tau = 345$ fs). Two longer-lived vibrations are also retrieved at 354 and 392 cm^{-1}, with dephasing timess of 465 and 742 fs, respectively. While specific assignments are again not possible, the short-lived, large amplitude modes observed here represent large scale skeletal torsions of the retinal molecule following absorption of a photon, and have been observed previously in both transient absorption[10] and DFWM[16] experiments.

4.5 Discussion

Quantifying the filtered transient vibrations confirms the observation that the probe region associated with the excited state at 525 nm does indeed contain a greater number of large amplitude, short dephasing time vibrational modes than the response at 630 nm. Many of these vibrations are not observed by techniques sensitive only to ground state vibrations such as Raman scattering[47,48]. These vibrations are (for $\lambda = 525$ nm, where the excited state modes are more pronounced) observed predominantly at 1633, 1220, 1097, 971, 869, 564, 226, and 195 cm^{-1}, frequencies which span the entire range from the highest frequency double bond stretches to low frequency collective torsional modes. Owing to the significant damping as a result of their short dephasing times, these modes would not figure prominently in power spectral analysis of transient response either, if the early delay times are neglected due to the coherent artifact which arises due to pulse overlap effects at zero delay between the pump and probe pulses. Due to the high optical purity of the nanodisc bR sample, we are able to perform measurements at low excitation conditions which minimize the coherent artifact, even for the short optical pulses used in the degenerate transient absorption measurements here. This allows for analysis of even the earliest time domain signals where the excited state vibrational dynamics are maximal.

In addition to the short dephasing time excited state dynamics, we observe all of the conventional high frequency ground state modes identified by previous ultrafast experiments. These are the long-lived vibrations due to ethylenic stretching at 1522 cm^{-1}, C-C stretches and associated rocking dynamics at 1281, 1198, and 1165 cm^{-1}, and the in-plane methyl rock at 1008 cm^{-1}, which gives further confidence in the Fourier filtering and subsequent time domain analysis for extracting coherent vibrational dynamics observed in ultrafast spectral measurements.

Unlike the amplitudes and dephasing times which were used in part to assign vibrations to either the excited or ground state potential energy surface, we observe no obvious trend in the retrieved phase values of the excited state modes about which to comment. For the ground state modes, we observe a similar relative phase shift for ground state modes[52] as reported by Kahan *et al.*[10].

While in general there is good agreement between previous measurements of the vibrational dynamics of retinal in bR following ultrafast excitation, we note three specific deviations from previous assignments: the highest frequency excited state stretching mode attributed to the Schiff base C=N bond at 1633 cm^{-1}, the methyl rock oscillation at 1008 cm^{-1}, and the low frequency torsional modes at $\sim$200 cm^{-1}.

First, the dynamics at $\sim$1640 cm^{-1} have previously shown activity in transient IR measurements[50] immediately following resonant excitation of bR in the purple membranes, with reactive modes showing a rise time of $\leq$ 500 fs at $\sim$ 1620 cm^{-1} and a long-lived ground state component at $\sim$ 1640 cm^{-1}. More recently, sliding window analysis of the transient absorption of purple membrane bR[11] indicated a C=N stretch mode at $\sim$1640 cm^{-1} persisting for a mere 30 fs following photolysis, a timescale less than two periods of oscillation of the mode in question. In the present work, we retrieve a mode at 1633 cm^{-1}, and find it decays with a time constant of 234 fs, in far better agreement with transient IR species observed at $\sim$ 1620 cm^{-1} than with either the ground state mode at $\sim$ 1640 cm^{-1} with a lifetime of over a picosecond, or with the sliding window analysis of resonant transient absorption signals with a 30 fs dephasing time. We do not observe a long dephasing time mode at these frequencies, and we speculate that the limitations imposed by the sliding window analysis may play a role in the discrepancy between our results and those of Yabushita *et al.*[11]

Second, the in-plane methyl rock at 1008 cm^{-1} identified originally as a ground state mode in Raman scattering experiments[47,48] was recently identified as a possible excited state vibration as a result of the spectral dependence of both the amplitude and width of this mode in power spectral analysis of DFWM signals[16]. In the present work the assignment is strictly that of a long-lived ground state mode, having a dephasing time on average of $\sim$ 700 fs. The presence of short-lived oscillations at a very similar frequency (971 cm^{-1} at the probe wavelength of 525 nm), is perhaps a complicating factor in the analysis by Kraack *et al.*[16], where a significant coherent artifact (exacerbated by the DFWM approach) required the exclusion the earliest temporal delays from analysis.

Third, the low frequency oscillation on the order of $\sim$ 200 cm^{-1} identified previously in both the resonant regime[10] and more recently with a near IR probe[53] are, in the present analysis, found to consist of not one dominant mode as was observed with a sliding window analysis in the near IR, but two closely spaced and roughly equal magnitude vibrations at 226 and 195 cm^{-1}, with decay constants on the order of $\sim$ 250 fs. This is in good agreement with the bandpass filtering results of Kahan *et al.*[10] in the resonant regime, whose approach inspired the present analysis. We also note with interest that the mode we recover at 226 cm^{-1} is in excellent agreement with the periodic oscillations retrieved from Wigner transformation of the optimal pulse determined by closed-loop weak field coherent control experiments on purple membrane bR[4], where an enhancement of the isomerization yield of retinal in bacteriorhodopsin following excitation with shaped pulses was attributed to a resonant interaction of the excitation field with low frequency vibrations active in the excited state. We find in the present analysis that the mode in question has a dephasing time and amplitude consistent with excited state origin.

Finally, we find our experimental results at odds with the model derived from femtosecond stimulated Raman spectroscopy[13] where Franck-Condon active modes such as the C=C and C-C stretches populate dark HOOP and torsional modes via intramolecular vibrational energy redistribution (IVR) on a $\sim$ 250 fs timescale. We find all of the coherent oscillations have maximal amplitudes at a zero probe delay, and find no evidence for a growth of vibrational transients at non-zero probe delays. The short temporal IRF (15 fs, which is shorter than a single period of even the 1633 cm^{-1} mode) and the minimal nonresonant contribution during pulse overlap afforded by the weak excitation conditions and optical purity of the nanodisc sample give confidence that the earliest transient signals are not contaminated by significant artifacts, and we are thus required to hypothesize an alternative mechanism for the population of these modes. One assumption common to the discussion of ground and excited state vibrational dynamics is that excited state frequency differences can be neglected[47], but this has previously been shown to fail for certain modes in other carotenoids, such as the C=C stretch of β-carotene[54–56]. It is thus plausible that the short dephasing time vibrational dynamics we observe are excited state analogues of ground state modes, with frequency shifts resulting from changes of the retinal chromophore in the excited state.

5 Conclusions

Upon reconstitution of bacteriorhodopsin trimers into lipid nanodiscs, we observe the characteristic linear spectral properties consistent with bR in the purple membranes, but with significantly reduced scattering due to the nanodisc microenvironment. Time domain spectroscopy on an ultrafast timescale to monitor the J and K photointermediate formation shows kinetics which are unchanged from the wild type purple membranes as well. On the microsecond to millisecond timescale, flash photolysis experiments reveal deviations from native kinetics for the later photointermediates involved in reprotona-

tion of the Schiff base and resetting of the photocycle, but no off-pathway intermediates were observed, indicating an otherwise native-like photocycle.

The vibrational dynamics of the retinal chromophore were subsequently studied by ultrafast degenerate transient absorption spectroscopy, where the modes were quantified using Fourier filtering and subsequent time domain fitting of the recovered vibrational transients. The use of nanodiscs for embedding bR was critical in this analysis. The dramatic reduction in scattering led to a greatly improved signal to noise ratio even for the weak excitation conditions employed in this study. The low fluence also effectively minimized non-resonant distortions about zero delays, and it was this feature which enabled analysis of the vibrational dynamics over the entire temporal window following photoexcitation. While many of the recovered excited state modes were not immediately assignable to known ground state vibrations, the long-lived modes were all assigned to vibrations identified by Raman scattering of the purple membrane bR.

Given the uncertain assignments of the excited state vibrational modes, we hope this inspires future work to compare with these results, both experimentally using novel spectroscopies specifically designed to resolve excited state vibrational modes[56,57], and computational and theoretical work to provide a better understanding of the excited state nuclear dynamics.

Note added in proof

Following submission of this paper, another transient absorption study of the vibrational dynamics in bacteriorhodopsin was published by Liebel *et al.*[58], with similar experimental results as presented here, but reach an alternative interpretation based on IVR from Raman active stretch modes to initially dark HOOP and torsional modes on a sub-50 fs timescale. This interpretation is not supported by our analysis, as we observe population of the breadth of excited state modes immediately following photoexcitation.

Acknowledgements

We would like to thank Prof. S. G. Sligar for the nanodisc trimeric bR figure template. This research was supported by the Natural Sciences and Engineering Research Council of Canada (R.J.D.M.), the Max Planck Society (R.J.D.M.), and the Canada Excellence Research Chair program (O.P.E.). O.P.E. is the Anne & Max Tanenbaum Chair in Neuroscience at the University of Toronto.

References

1 O. P. Ernst, D. T. Lodowski, M. Elstner, P. Hegemann, L. S. Brown and H. Kandori, *Chemical Reviews*, 2014, **114**, 126–163.
2 R. A. Mathies, C. H. Brito Cruz, W. Pollard and C. V. Shank, *Science*, 1988, **240**, 777–779.
3 J. Dobler, W. Zinth, W. Kaiser and D. Oesterhelt, *Chemical Physics Letters*, 1988, **144**, 215–220.
4 V. I. Prokhorenko, A. M. Nagy, S. Waschuk, L. S. Brown, R. R. Birge and R. J. D. Miller, *Science*, 2006, **313**, 1257–1261.
5 V. I. Prokhorenko, A. M. Nagy, L. S. Brown and R. J. D. Miller, *Chemical Physics*, 2007, **341**, 296–309.
6 S. L. Dexheimer, Q. Wang, L. Peteanu, W. Pollard, R. A. Mathies and C. V. Shank, *Chemical Physics Letters*, 1992, **188**, 61–66.
7 W. Pollard, S. L. Dexheimer, Q. Wang, L. Peteanu, C. V. Shank and R. A. Mathies, *Journal of Physical Chemistry*, 1992, **96**, 6147–6158.
8 T. Kobayashi, T. Saito and H. Ohtani, *Nature*, 2001, **414**, 531–534.
9 D. M. Jonas, S. E. Bradforth, S. A. Passino and G. R. Fleming, *Journal of Physical Chemistry*, 1995, **99**, 2594–2608.
10 A. Kahan, O. Nahmias, N. Friedman, M. Sheves and S. Ruhman, *Journal of the American Chemical Society*, 2007, **129**, 537–546.
11 A. Yabushita and T. Kobayashi, *Biophysical Journal*, 2009, **96**, 1447–1461.
12 G. I. Groma, A. Colonna, J.-L. Martin and M. H. Vos, *Biophysical Journal*, 2011, **100**, 1578–1586.
13 D. W. McCamant, P. Kukura and R. A. Mathies, *Journal of Physical Chemistry B*, 2005, **109**, 10449–10457.
14 S. Shim, J. Dasgupta and R. A. Mathies, *Journal of the American Chemical Society*, 2009, **131**, 7592–7597.
15 K. Niu, B. Zhao, Z. Sun and S.-Y. Lee, *Journal of Chemical Physics*, 2010, **132**, 084510.
16 J. P. Kraack, T. Buckup, N. Hampp and M. Motzkus, *Chemphyschem : a European journal of chemical physics and physical chemistry*, 2011, **12**, 1851–1859.
17 N. R. Civjan, T. H. Bayburt, M. A. Schuler and S. Sligar, *BioTechniques*, 2003, **35**, 556–60– 562–3.
18 T. H. Bayburt, Y. V. Grinkova and S. Sligar, *Archives of Biochemistry and Biophysics*, 2006, **450**, 215–222.
19 T. H. Bayburt, A. J. Leitz, G. Xie, D. D. Oprian and S. Sligar, *Journal of Biological Chemistry*, 2007, **282**, 14875–14881.
20 H. Tsukamoto, A. Sinha, M. DeWitt and D. L. Farrens, *Journal of Molecular Biology*, 2010, **399**, 501–511.
21 A. Pandit, N. Shirzad-Wasei, L. M. Wlodarczyk, H. van Roon, E. J. Boekema, J. P. Dekker and W. J. de Grip, *Biophysical Journal*, 2011, **101**, 2507–2515.
22 T. K. Ritchie, Y. V. Grinkova, T. H. Bayburt, I. G. Denisov, J. K. Zolnerciks, W. M. Atkins and S. Sligar, *Methods in Enzymology*, 2009, **464**, 211–231.
23 M. J. Ranaghan, C. T. Schwall, N. N. Alder and R. R. Birge, *Journal of the American Chemical Society*, 2011, **133**, 18318–18327.
24 J. Wang, J. Sasaki, A.-L. Tsai and J. L. Spudich, *Journal of Biological Chemistry*, 2012, **287**, 21316–21325.
25 R. Casadio and W. Stoeckenius, *Biochemistry*, 1980, **19**, 3374–3381.
26 N. A. Dencher, K.-D. Kohl and M. P. Heyn, *Biochemistry*, 1983, **22**, 1323–1334.
27 J. Wang, S. Link, C. D. Heyes and M. A. El-Sayed, *Biophysical Journal*, 2002, **83**, 1557–1566.
28 T. H. Bayburt, Y. V. Grinkova and S. Sligar, *Nano Letters*, 2002, **2**, 853–856.
29 V. I. Prokhorenko, A. Halpin, P. J. M. Johnson, R. J. D. Miller and L. S. Brown, *Journal of Chemical Physics*, 2011, **134**, 085105–.
30 I. van Stokkum, D. S. Larsen and R. van Grondelle, *Biochimica et biophysica acta*, 2004, **1657**, 82–104.
31 S. Waschuk, A. G. Bezerra Jr., L. Shi and L. S. Brown, *Proceedings of the National Academy of Sciences of the United States of America*, 2005, **102**, 6879–6883.

32 A. K. Dioumaev, *Biophysical Chemistry*, 1997, **67**, 1–25.

33 P. J. M. Johnson, V. I. Prokhorenko and R. J. D. Miller, *Optics Letters*, 2011, **36**, 2170–2172.

34 P. Altoè, A. Cembran, M. Olivucci and M. Garavelli, *Proceedings of the National Academy of Sciences of the United States of America*, 2010, **107**, 20172–20177.

35 J. B. Ames and R. A. Mathies, *Biochemistry*, 1990, **29**, 7181–7190.

36 K. Ludmann, C. Gergely and G. Váró, *Biophysical Journal*, 1998, **75**, 3110–3119.

37 A. H. Xie, J. F. Nagle and R. H. Lozier, *Biophysical Journal*, 1987, **51**, 627–635.

38 I. Chizhov, D. S. Chernavskii, M. Engelhard, K.-H. Mueller, B. V. Zubov and B. Hess, *Biophysical Journal*, 1996, **71**, 2329–2345.

39 H. Otto, T. Marti, M. Holz, T. Mogi, L. Stern, F. Engel, H. G. Khorana and M. P. Heyn, *Proceedings of the National Academy of Sciences of the United States of America*, 1990, **87**, 1018–1022.

40 G. Váró and J. K. Lanyi, *Biochemistry*, 1991, **30**, 7165–7171.

41 O. Kalisky, C. R. Goldschmidt and M. Ottolenghi, *Biophysical Journal*, 1977, **19**, 185–189.

42 C. Gergely, C. Ganea and G. Váró, *Biophysical Journal*, 1994, **67**, 855–861.

43 M. Etzkorn, T. Raschle, F. Hagn, V. Gelev, A. J. Rice, T. Walz and G. Wagner, *Structure*, 2013, **21**, 394–401.

44 S. Subramaniam and R. Henderson, *Nature*, 2000, **406**, 653–657.

45 T. Hirai and S. Subramaniam, *PLOS ONE*, 2009, **4**, e5769.

46 F. J. Harris, *Proceedings of the IEEE*, 1978, **66**, 51–83.

47 A. B. Myers, R. A. Harris and R. A. Mathies, *Journal of Chemical Physics*, 1983, **79**, 603–613.

48 S. O. Smith, M. S. Braiman, A. B. Myers, J. A. Pardoen, J. M. L. Courtin, C. Winkel, J. Lugtenburg and R. A. Mathies, *Journal of the American Chemical Society*, 1987, **109**, 3108–3125.

49 C. J. Bardeen, Q. Wang and C. V. Shank, *Journal of Physical Chemistry A*, 1998, **102**, 2759–2766.

50 J. Herbst, K. Heyne and R. Diller, *Science*, 2002, **297**, 822–825.

51 F. L. Gervasio, G. Cardini, P. R. Salvi and V. Schettino, *Journal of Physical Chemistry A*, 1998, **102**, 2131–2136.

52 A. T. N. Kumar, F. Rosca, A. Widom and P. M. Champion, *Journal of Chemical Physics*, 2001, **114**, 701.

53 A. Wand, B. Loevsky, N. Friedman, M. Sheves and S. Ruhman, *Journal of Physical Chemistry B*, 2013, **117**, 4670–4679.

54 H. Hashimoto and Y. Koyama, *Chemical Physics Letters*, 1989, **154**, 321–325.

55 W. Fuß, Y. Haas and S. Zilberg, *Chemical Physics*, 2000, **259**, 273–295.

56 J. P. Kraack, A. Wand, T. Buckup, M. Motzkus and S. Ruhman, *Physical Chemistry Chemical Physics: PCCP*, 2013, **15**, 14487.

57 M. Liebel and P. Kukura, *Journal of Physical Chemistry Letters*, 2013, **4**, 1358–1364.

58 M. Liebel, C. Schnedermann, G. Bassolino, G. Taylor, A. Watts and P. Kukura, *Physical Review Letters*, 2014, **112**, 238301.